Water Vapor Condensation on Bio-inspired Patterned Structures

Samuel Thomas

This report presents combined simulation and experimental investigations of water vapors condensing on patterned surfaces, with the purpose of evaluating the efficacy of simulated results for predicting condensation on patterned surfaces. The simulation utilizes the k-epsilon model for turbulence as well as Lee model condensation in ANSYS Fluent Computational Fluid Dynamics (CFD) package. Three types of patterning are utilized, including cubes (square bumps), semicircles (circular bumps), and cones (triangular spikes), with a non-patterned control case. The results illustrate that patterns with higher surface area result in higher liquid condensation. The simulation results show that a maximum water condensation of 1.2844e-003 grams over 10 seconds and 35 mm^2 happened on the Square Bumps structure surface, and experimental results confirmed this with an average water condensation of 5.4156 grams for the same surface, which was also the highest yield for the experimental trials.

Background

From self-cleaning mechanisms to drawing moisture from the air to collect water in drought-stricken regions, studying condensation behavior on patterned surfaces has a number of far-reaching applications. The implications of this work would benefit a range of applications, including assisting in the harvesting of water vapors to produce drinkable water for drought-stricken areas, as well as various processes involved in harvesting and dispersing energy such as nuclear energy and HVAC. Lapotin et al., for example, utilized a copper condenser within their dual stage water harvesting device for heat rejection, which could benefit from a patterned surface to increase the efficiency of this process (1). Several examples of these behaviors are present in nature. The Namib Beetle condenses moisture on its wings to drink (2), and the Lotus Leaf uses condensation to wash away contaminants (3). Considering the impacts of the COVID-19 pandemic,, it has become difficult to study these behaviors in person. However, using CFD, condensation can be simulated in an affordable and efficient manner, and the results can then be adapted into realistic scenarios.

The phase change model proposed by Lee (4) is widely utilized in CFD, and posits that the rate of mass transfer, "ṁ," will be dependent upon the volume fraction of a phase, the density of the mixture, and the proportion of the temperature above or below the saturation temperature to the saturation temperature, and is described in Equations 1 and 2:

$$\dot{m}_l = c_1 v_f \rho \, \frac{T_s - T}{T_s}, \text{for condensation} \tag{1}$$

$$\dot{m}_v = c_2 v_f \rho \, \frac{T_s - T}{T_s}, \text{for evaporation} \tag{2}$$

Where "c_1" and "c_2" represent the condensation and evaporation frequencies respectively, "v_f" represents volume fraction,"ρ" is mixture density, "T" is temperature, and "T_s" is the saturation temperature. "c_1" and "c_2" are tweaked to fit experimental data. This equation is applied to every element to determine the volume of each phase within the control volume over time.

In order to focus on the effects of the surface patterning on condensation due to heat flux, most conditions are left as defaults save for surface temperature, fluid temperature, inlet temperature, and inlet velocity. This setting creates a situation where condensable gas heated above the saturation point is constantly introduced into the control volume, causing mass transfer due to the temperature difference. The results of this work demonstrate a positive

correlation between surface area and mass generation which is supported by data from physical trials and reveal the potential for similar work with patterned surfaces that maximize the effectiveness of moisture condensing devices.

Objectives

The purpose of this project is to simulate condensation on patterned surfaces using ANSYS Fluent CFD software and experimentally test the patterned surface for water condensation at a given temperature difference and humidity to understand the effect of surface structures on moisture condensation. These experiments will be used to evaluate the validity of the model proposed in this work towards the overall goal of verifying the extent to which CFD can be used to predict heat and mass transfer for condensation over varying geometries, and how to optimize models to better predict this behavior.

Methods

Equipment and Materials

A computer running ANSYS Fluent application is used for simulation work. A MiiCraft Ultra 150 Digital Light Processing (DLP) 3D printer is used with FunToDo Snow White UV curing resin to fabricate surfaces for experimental work. A Juragon RX incubator is used to maintain a warm and humid environment while a Julabo HE circulator circulates ethylene glycol cooled by a U-Cool external bath cooler, generating a temperature difference. A laboratory balance is used to collect data from experimental trials.

Procedures

Simulation Work

Three different geometries are designed to test patterning's effect on the condensation of vapor: square pillars (square bumps), hemispheric pillars (circular bumps), and cones (triangular spikes). The first geometry is for calibration purposes; establishing maximum element sizing and spacing for each patterning (in other words, the element sizes of the other pillars may not be larger than the square bumps pillars in any direction). The bumps are inspired by the bumps of the Namiib beetle, while the cones are akin to the peaks and valleys of the lotus leaf.

Using ANSYS DesignModeler, a 5 mm height, 2.5 mm base length trapezoidal plane with 45° sloped leg and vertical leg is extruded by 5 mm. This geometry is frozen, and a plane is generated to coincide with the sloped side to generate geometries. For the square bumps geometry, a pattern of 0.5 mm cubes is generated. Triangular spikes are generated by revolving 0.25 mm by 0.5 mm height right triangles about the longest side. Circular bumps are semicircles revolved about a straight edge corresponding to a diameter of 0.5 mm.

Each geometry patterns the condenser with five rows and seven columns, spaced 0.25 mm from the bottom and adjacent sides and 0.5 mm between each body. These bodies are cut out of the control volume by using the enclosure tool. The surface area of the condenser (sloped edge) is 35.355 mm^2 for the flat surface, while the square bumps patterned condenser is 69.301 square mm, the triangular spikes patterned condenser is 43.854 square mm, and the circular bumps patterned condenser is 42.175 mm^2. Because several objects in the square bumps surface do not fit in the control volume, the patterning is insignificantly cut off. This is done for the sake of uniformity, as opposed to expanding the control volume or removing the top row from each case. Maximum element size or length is limited to a minimum of 0.5 mm due to computational limitations. Figure 1 demonstrates the geometries used in this procedure:
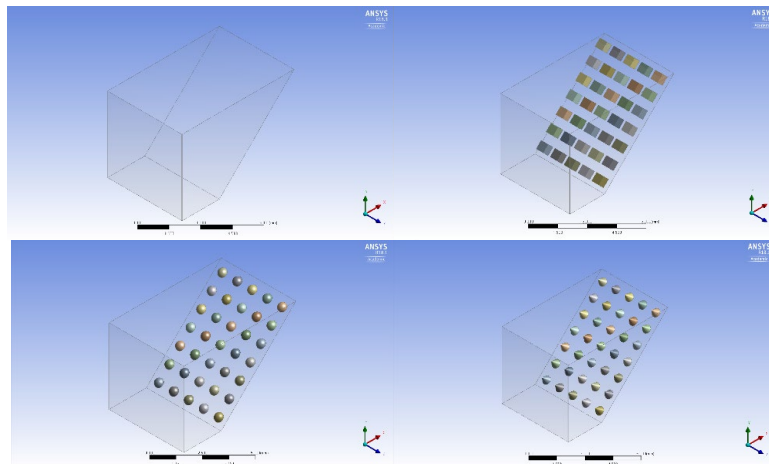

Figure 1: Geometries used in simulation work. From top left to bottom right: flat surface, square bumps, circular bumps, and triangular spikes.

Using ANSYS Meshing Tool, 0.5 mm is specified for maximum face and tetrahedral size, while face sizing is applied at the condenser. Named selections are chosen, with the sloped side set to condenser, the bottom side (towards the negative "Y" axis) set to outlet, the vertical side (opposite the condenser) set to inlet, and all other sides set to symmetric. For the flat surface case, the mesh is hexahedral to lower the skewness and increase the quality of the mesh as the

simplicity of the design permits this. As a result, a sizing of 0.1 mm is used. For all other cases, the patterning causes the program to use a tetrahedral mesh, which creates a finer mesh. To save on computational costs, a sizing of 0.25 mm is used at the condenser. Figure 2 displays the mesh for each case:
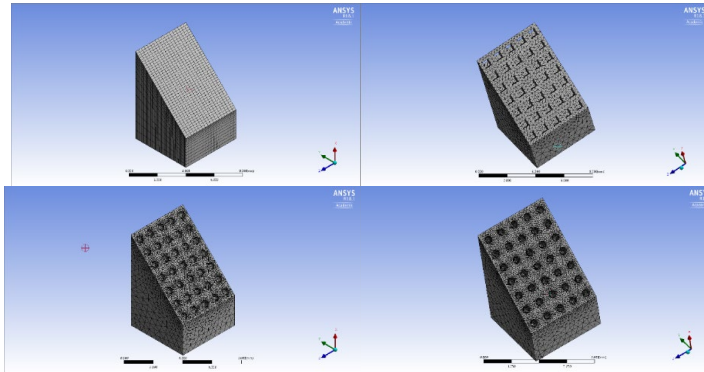

Figure 2: Meshing for each case. From top left to bottom right: flat surface, square bumps, circular bumps, and triangular spikes. A hexahedral mesh is used for the flat surface case as this geometry is the simplest. A tetrahedral mesh is utilized for patterned surfaces. To account for the curvature in the Circular Bumps and Triangular Spikes patterns, the mesh is finer at the condenser, and because of the sharp points in the Triangular Spikes patterning, the mesh is finest in this case.

In Fluent, the time condition is set to transient, and gravity set to -9.81 $\frac{m}{s^2}$ in the Y direction. The energy equation is enabled, and the viscous model is set to k-epsilon, with enhanced wall treatment, viscous heating, and thermal effects enabled. Multiphase is set to VOF with implicit body force, sharp or dispersed interface modeling, zonal discretization, and phase localized discretization enabled. Water liquid and water vapor are added as materials, as well as copper, with phase one set to water vapor, and phase two set to liquid under the phase dialog box. Mass transfer is set from liquid to vapor, evaporation-condensation with a condensation frequency of 50. Surface tension modeling is set to constant, with wall adhesion and jump adhesion activated, and 0.06 $\frac{N}{m}$ set for the constant. Phase localized compressive scheme is set under discretization. Under the boundary conditions the condenser temperature is set to 273 ˚K with material specified as copper, and inlet temperature is set to 380 ˚K, with velocity set to 0.1 $\frac{m}{s}$, and volume fraction of liquid set to 0. The fluid body is initially set to 380 ˚K and zero volume fraction for liquid. The data file is set to save every 20 timesteps, with quantities for liquid and vapor fraction set to save to the data file, as well as the mass transfer rate. Timestep is set to 0.01 s, with 1000 timesteps.

Experimental Tests

To verify the results of the Fluent simulations, a MiiCraft Ultra 150 DLP printer is used to produce the various patterned surfaces with FunToDo Snow White resin. For each print, a layer size of 50 micron is adapted, with a cure time ranging from 1.25 to 2.5 seconds, depending on quality of features. Due to the resin being unoptimized for smaller layer sizes than 50 microns with the MiiCraft printer, some defeaturing was observed, as the Triangular Spikes pattern was subject to a lower taper than required, and the curvature on the Circular Bumps was not encapsulated very well. Figure 3 demonstrates the geometry of each surface:
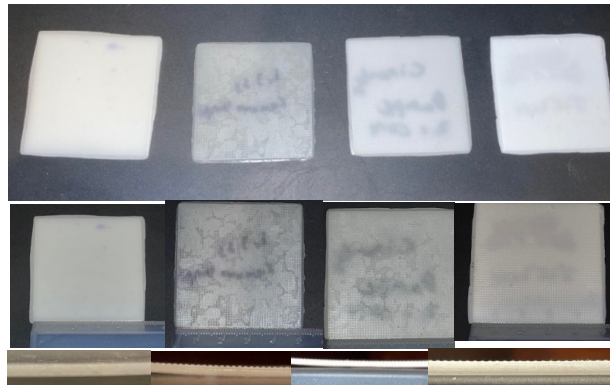

Figure 3: Patterned surfaces after printing. Left to right: flat surface, square bumps, circular bumps, and triangular spikes. Each surface is displayed with respective overall dimensions and side view below each sample. Defeaturing can be observed on Circular Bumps and Triangular Spikes surfaces.

To create the conditions necessary for physical tests, a Julabo HE model circulator circulates ethylene glycol through vinyl tubing, while an external compressor reduces the bath temperature below -5 ˚C, a Juragon RX incubator produces a hot, humid environment above 40 ˚C and 60% relative humidity (rH), and an ultrasonic nebulizer provides supplementary moisture to maintain this rH. Figure 4 demonstrates the equipment used for physical trials:

Figure 4: Equipment used for physical trials of each surface. From left to right: MiiCraft Ultra 150 DLP Printer, Julabo HE Circulator, U-Cool external chiller, Ultrasonic Nebulizer, and incubator with small vial of distilled water and pump to maintain humidity. A beaker of distilled water is kept on hand to refill humidity generating components.

Before each trial, a collecting tray and the surface are weighed to establish an initial weight. During trials for each surface, bath fluid is pumped through a copper plate within the incubator, cooling down the surface and allowing for condensation through convection between the surface and the fluid within the incubator. After 15 minutes, the surface is removed from the plate and placed into the tray, which collects moisture condensed on the surface over the trial. These two components are then weighed and compared to the initial weight to establish the amount of liquid condensed on the surface. Figure 5 demonstrates an example of data collection and surfaces post trial:
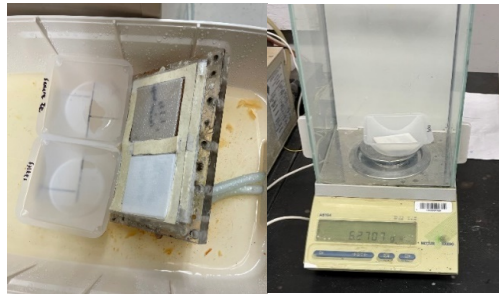

Figure 5: Copper plate and trays used to collect liquid (left), as well as balance used to collect data.

Results and Discussion

Simulation Work Results

The behavior of liquid that condenses on the surface of the condenser is reasonable for the scenario being modeled. As vapor enters the control volume at the inlet at 0.1 m/s, it is cooled below the saturation temperature at the condenser, forming droplets that bead up and roll off, exiting through the outlet. This is demonstrated in Figures 6 and 7:
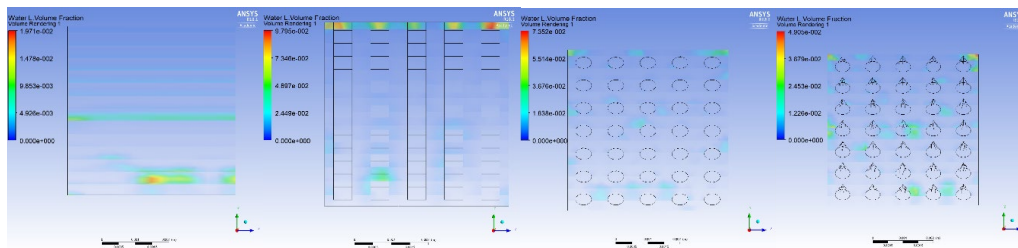

Figure 6: Volume rendering of liquid volume fraction of liquid water for all cases at t = 10 seconds. From top left to bottom right, flat surface, square, circular, and triangular cases.
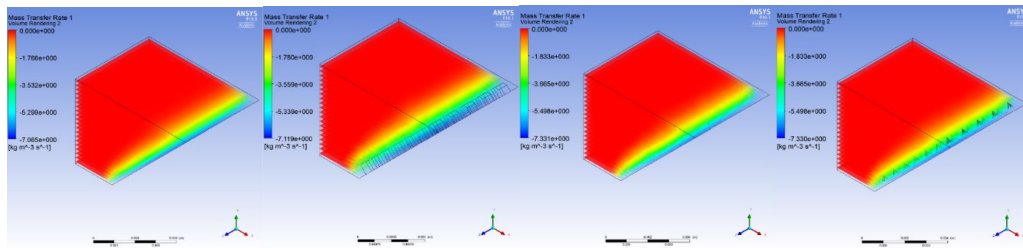
Figure 7: Volume rendering of mass transfer rate 1 for all cases at t = 10 seconds. From top left to bottom right, flat surface, square, circular, and triangular cases. The mass transfer rate of liquid is negative.

The mass transfer rate peaks at the condenser due to the temperature difference between the surface and the fluid, corresponding to the temperature boundary layer as a result. Figure 8 demonstrates a volume rendering of temperature for each case, demonstrating similar patterning to the rendering of the mass transfer rate for each case:
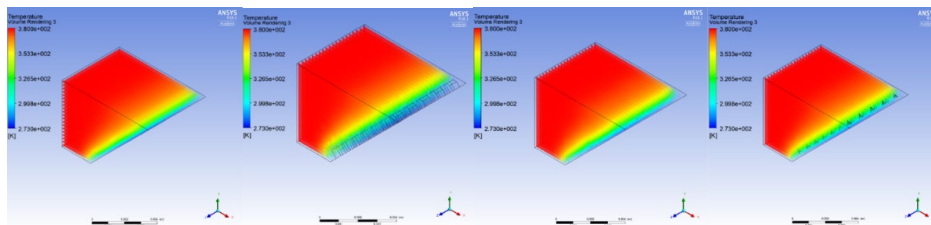

Figure 8: Volume rendering of temperature for all cases at t = 10 seconds. From top left to bottom right, flat surface, square, circular, and triangular cases.

Higher liquid mass transfer rates are observed in circular bumps and triangular spikes cases (-7.330 and -7.331, respectively), which is likely due to the finer elements in these meshes, as mass transfer rate is calculated in each cell based on volume and mass generation (units are $\frac{kg}{m^3 * s}$). Because the solver works based on the finite volume method, where a control volume is broken down into a computational domain consisting of a mesh of finer volume elements to calculate over, a finer mesh will have smaller elements at the condenser for this situation, and as a result, these areas will be cooled more than elements of a coarser mesh, as this will have larger elements at the condenser, similar to burning a wood chip as opposed to a log. As such, according to Equation 1, this element will have a higher rate of mass transfer, although on average (over an array of finer mesh elements that have the same volume/location as an element from a coarser mesh) the two scenarios should have similar rates. Figures 6 through 8 demonstrate that the simulation work show patterns for droplet accumulation, temperature boundary layer formation, and contour for mass transfer rate that follow trends observable in real life.

The graphs pictured below in Figure 9 are the result of integrating mass transfer rate over the control volume, articulated by Equation 3:

$$\dot{m}_{total} = \int_0^V \dot{m}'''_v - \dot{m}'''_l \, dV \tag{3}$$

where, "$\dot{m}_{total}$" represents the total mass transfer over the volume, $\dot{m}'''_v$ represents vapor mass generation over the volume in $\frac{kg}{m^3 * s}$, $\dot{m}'''_l$ represents liquid mass generation over the volume in $\frac{kg}{m^3 * s}$, and "V" represents volume in m^3:
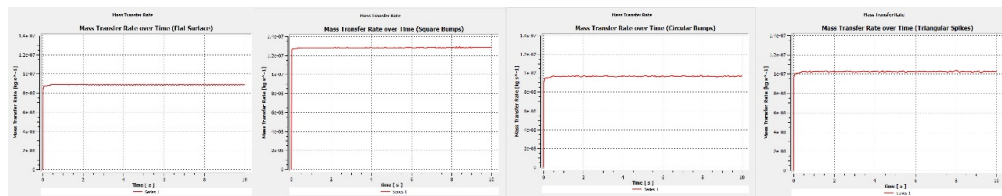

Figure 9: Plot of liquid mass generation over time for all cases over 10 seconds. From top left to bottom right, flat surface, square, circular, and triangular cases.

Liquid generation can be considered constant in all cases, as the graph of liquid generation over time demonstrates that the curve only minutely oscillates about a value. As a result, the following equation can be used to find the total mass generation over time:

$$m_{total} = \int_0^t \dot{m}_{total} \, dt = \dot{m}_{total} * t + C \tag{4}$$

where, "m_{total}" represents total liquid mass in kg, "t" represents time in seconds, and "C." the constant of integration, is zero, as no mass exists in the control volume at t = 0. The subsequent graph of this equation confirms this, as it is almost completely linear as seen in Figure 10:
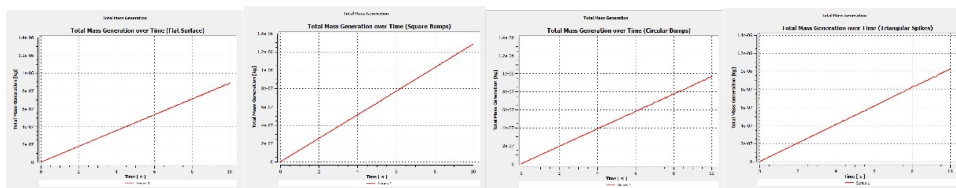

Figure 10: Plot of liquid mass generation over time for all cases over 10 seconds. From top left to bottom right, flat surface, square, circular, and triangular cases.

Table 1 summarizes the results of these calculations:

	Mass Generation Rate (kg/s)	Total Mass Generation (kg)	Condenser Surface Area (mm^2)
Flat Surface	$8.88921e-008$	$8.88921e-007$	35.355
Square Bumps	$1.2844e-007$	$1.2844e-006$	69.301
Circular Bumps	$9.68302e-008$	$9.68303e-007$	42.175
Triangular Spikes	$1.0291e-007$	$1.0291e-006$	43.854

Table 1: Mass generation rate and total mass generation for each case, at t = 10 s

This is consistent with conceptual predictions of condensation efficiency, as higher surface area should allow for a higher amount of heat transfer with the fluid body, and the results appear follow a linear trend with surface area, as demonstrated by the following plot in Figure 11:
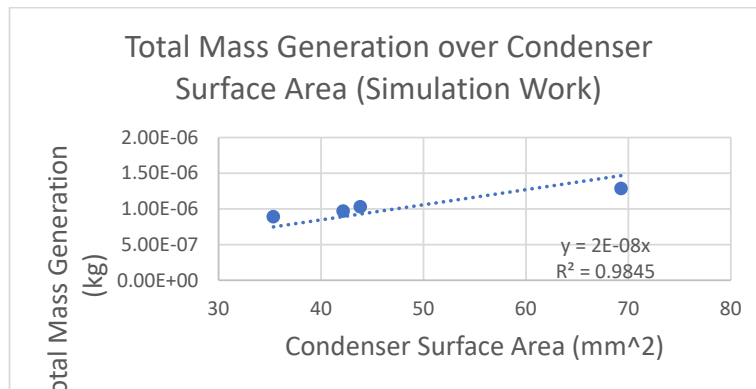

Figure 11: Plot of total mass generation over condenser surface area with intercept set at 0 for simulated trials.

Experimental Test Results

The setup used for testing and the trials vary by several factors. The surfaces involved in physical trials being composed of polymer should lower the rate of heat transfer between the fluid and the surface, governed by Nusselt number. The Nusselt number represents the ratio of convective to conductive heat transfer, and is demonstrated in Equation 5 (5):

$$Nu_{ave,L} = \frac{hL}{k} = 0.664\, Re_L^{\frac{1}{2}} Pr^{\frac{1}{3}} \quad (Pr > 0.6) \tag{5}$$

where, "$Nu_{ave,L}$" is the average Nusselt number over the entire surface, "h" is the heat transfer coefficient, "L" is the length of the surface, "k" is the thermal conductivity of the surface, "Re_L" is Reynolds number for the surface, and "Pr" is the Prandtl number for the fluid. Although data for the thermal conductivity of the resin are not available, thermal conductivity for plastics in general tend to be below $1 \frac{W}{m*K}$, while copper is well known to have a thermal conductivity of over $400 \frac{W}{m*K}$ (6). Because plastic thermal conductivity is much lower, it should be safe to assume that there will be a much lower rate of heat transfer due to a lower heat transfer coefficient, as Reynolds number and Prandtl number will be the same, and length of surface will be the same (if the same condenser area is considered), leading to a lower heat transfer coefficient for the surface.

Additionally, the temperature of the fluid in the environment is much lower at around 40 ˚C and relative humidity is slightly above 60% (resulting in a vapor volume fraction of closer to 0.044), compared to the 100 ˚C saturated vapor used in the simulations. The coolant is also at a much lower temperature initially, below -5 ˚C, but the reason the coolant is significantly cooled is because the use of an external chiller prevents active cooling of the fluid while pumping. As a result, the temperature of the fluid rose to 5 ˚C after 15 minutes of pumping, preventing the condenser from being maintained at a temperature of 0 ˚C. All of these factors should lead to a reduced yield when considering a scaled-up version of the model.

Table 2 summarizes the results of testing each surface using previously mentioned setup under the *Experimental Trials* section of the procedure, and Table 3 summarizes the measured conditions for each trial:

	Initial (g)	Final (g)	Condensed Water (g)	Average Condensed Water (g)	Standard Deviation (g)
Flat Surface	6.1517	6.4375	0.2858	0.4424	0.1743
	6.1679	6.5791	0.4112		
	6.1704	6.8006	0.6302		
Square Bumps	5.7857	12.6108	6.8251	5.4156	3.0028
	5.7875	13.2419	7.4544		
	5.7928	7.7602	1.9674		
Circular Bumps	6.1988	6.4424	0.2436	3.2148	2.5795
	6.1998	11.0804	4.8806		
	6.2189	10.7392	4.5203		
Triangular Spikes	6.2790	6.7161	0.4371	3.3013	2.6105
	6.2707	11.8176	5.5469		
	6.2750	10.1948	3.9198		

Table 2: Condensed water in experimental trials of each surface.

	Internal Temp Before (°C)	rH Before (%)	Bath Temp Before (°C)	Internal Temp After (°C)	rH After (%)	Bath Temp After (°C)
Flat Surface	40.4	66	-6.05	41	57	4.51
	41	67	-5.68	41.4	48	5.54
	40.1	67	-5.51	41.8	62	5.1
Circular bumps	40.4	65	-6.05	38.9	56	5.77
	40.7	60	-5.56	41.9	61	4.84
	40.4	67	-5.86	41.7	61	4.76
Spines	40.2	61	-4.51*	41.8	62	4.69
	41.2	64	-5.63	41.9	60	5.35
	41.3	62	-5.76	41.9	56	4.94
Square	40.4	66	-6.05	41	57	4.51
	40.1	62	-5.29	41.8	52	5.09
	40	62	-5.46	41.1	62	4.93
Average	40.5167	64.0833	-5.6175	41.35	57.8333	5.0025
Standard Deviation	0.4387	2.5746	0.4283	0.8501	4.4279	0.3923

Table 3: Conditions within the environment for each trial. Marked value (*) was recorded slightly after pumping, but the bath was cooled below -5 °C in this case.

The average liquid condensation yields for each surface are positively correlated with surface area, as predicted by the simulations. Variations in condensed water may be explained by variations in conditions within the incubator, possibly by poor contact with the copper plate for certain trials due to condensed liquid on the plate. However, the overall efficiency for each surface should be well encapsulated by the mean, as most data falls within one standard deviation (2 out of 3 trials for each surface), and all data falls within two. Additionally, the data in Table 3 demonstrates that the standard deviation of the mean for temperature readings falls below 0.5 °C for bath temperature and internal temperature, apart from internal temperature after each trial, which is below 1 °C and could be related to surface performance. The data in Table 2 is encapsulated in the graph in Figure 12:
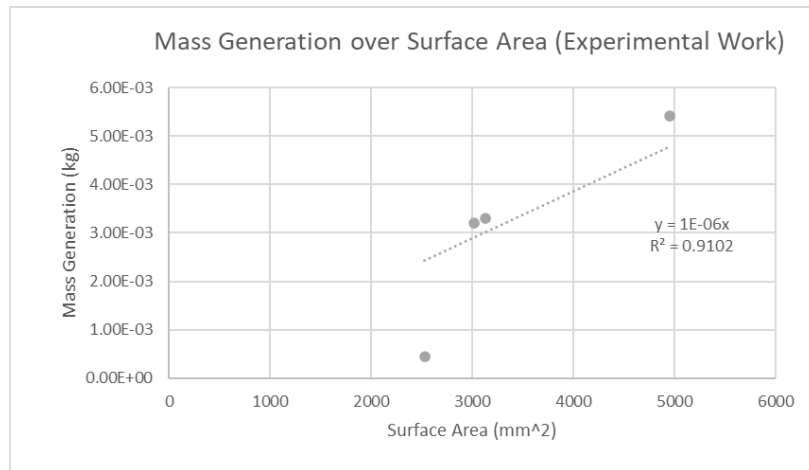
Figure 12: Average mass generation plotted against surface area for physical trials of each surface.

As demonstrated by the chart, average mass generation increases as the surface area of the condenser increases. Given that the R^2 value of the data is 0.9102, the data is mostly dependent on surface area, but with more variation due to other factors than the simulated data, which had an R^2 value of 0.9845. However, the slope of the trendline is $1e-06\frac{kg}{mm^2}$, as opposed to the simulated data, which has a slope of $2e-08\frac{kg}{mm^2}$. Accounting for the difference in simulated time compared to that of the physical trials (15 minutes as opposed to 10 seconds, so scale up by a factor of 90) and scaling up to the surface area of the condenser (scale up by a factor of 2500 mm^2 to 35 mm^2, the product of the edge lengths for the physical surfaces and the surfaces in the computational domain, respectively) for each surface that was simulated, the slope of the chart of liquid condensed in simulations should be $2e-06\frac{kg}{mm^2}$, which is demonstrated by the following chart in Figure 13:
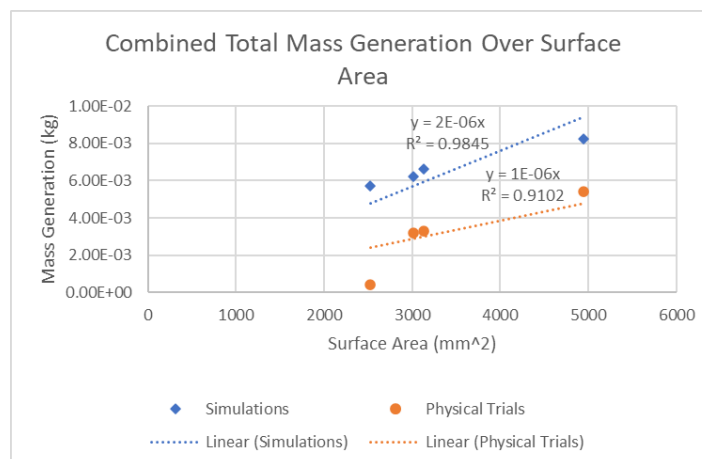

Figure 13: Combined data for simulation work and experimental trials.

Based on the Nusselt number of the surface, the efficiency of the simulations should be over 400 times the efficiency of the physical trials. Regardless, as demonstrated by this data, the simulation predicts the results of experimental trials to an unprecedented degree, as the simulation work predicts about double the condensation of the physical trials, while a much lower condensation efficiency (400 times less than simulated data) should have been recorded when accounting for the material difference. It is possible that there are some effects that scale up with the control volume under consideration, such as liquid that condenses off the surface (or in other parts of the incubator), or are otherwise unaccounted for in the simulation, such as areas of poor circulation/saturation and condensed liquid from other areas of the condenser. As a result of these discrepancies, for more accurate prediction for condensation behavior, a more complicated simulation using a larger control volume/surface, appropriate material properties for the condenser surface, and more faithful conditions should be tested. This would imply accounting for an air phase with a lower vapor fraction according to rH at room temperature in this case, but could be adjusted to fit the scenario for other purposes as well; a power plant may need to model at higher rH and temperature, for example.

Conclusions

Using ANSYS Fluent CFD software is an efficient and cost-effective way to model condensation. Trends observed in this work are applicable to real life situations, as they demonstrate observable patterns in nature, such as boundary layer formation, droplet accumulation, and a strong correlation between surface area and condenser efficiency. However, when predicting specific values for condensation, a model more accurate to the situation would be necessary, as variations in conditions such as condenser material, temperature difference, and relative humidity likely caused a lower condensation frequency for the surfaces in experimental trials, strictly speaking about heat transfer condensation. When it comes to the efficiency of each surface modeled in this work, it seems that the results are too similar, as the aforementioned factors should lower the efficiency of each surface significantly. As discussed previously, effects such as liquid condensing in other regions of the control volume, areas of poor saturation or circulation, and liquid from other areas of the condenser may also play a role in lowering condensation frequency, but due to unpredictability, computing limitations, or both, may not be well accounted for in simulation work. In general, the model used in this work should be effective to test the efficiency of surface patterning comparatively as a baseline, while a more accurate model may be required to predict performance of surface condensation efficiency experimentally, which should conform to the specific application being studied and the conditions being replicated in each work.

REFERENCES

1. LaPotin, A., Zhong, Y., Zhang, L., Zhao, L., Leroy, A., Kim, H., Rao, S. R., & Wang, E. N. (2021). Dual-stage atmospheric water harvesting device for scalable solar-driven water production. *Joule*, 5(1), 166–182. https://doi.org/10.1016/j.joule.2020.09.008

2. Ensikat, H. J., Ditsche-Kuru, P., Neinhuis, C., & Barthlott, W. (2011). Superhydrophobicity in perfection: The outstanding properties of the lotus leaf. *Beilstein Journal of Nanotechnology*, 2, 152–161. https://doi.org/10.3762/bjnano.2.19

3. Sun, J., & Bhushan, B. (2012). Structure and mechanical properties of beetle wings: A review. *RSC Advances*, 2(33), 12606-12623. https://doi.org/10.1039/c2ra21276e

4. Lee, W. H. (2013). Computational methods for two-phase flow and particle transport. *WORLD SCIENTIFIC*. https://doi.org/10.1142/8683

5. Bergman, T. L., & Lavine, A. (2017). *Fundamentals of heat and mass transfer*. John Wiley & Sons.

6. Eiermann, K., & Hellwege, K. -xH. (1962). Thermal conductivity of high polymers from −180°C. to 90°C. *Journal of Polymer Science*, 57(165), 99–106. https://doi.org/10.1002/pol.1962.1205716508

Author

Samuel Thomas

Samuel Thomas is a Mechanical Engineering student at Villanova with minors in Biomedical Engineering and Mechatronics. As a member of the class of 2022, he has worked on several projects ranging from CFD simulation to data acquisition and analysis. He is the President of Villanova ASME, as well as the president and co-founder of the Villanova Chess Club.
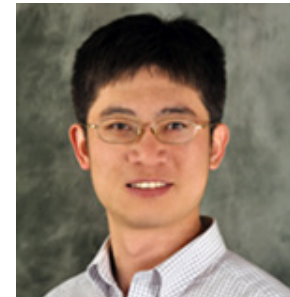
Mentor

Dr. Calvin Li

Dr. Calvin Li is an associate professor in the Department of Mechanical Engineering at Villanova University. Dr. Li has extensive research experience in thermal management, advanced nanomaterials and structures, and renewable energy, and worked with many excellent graduate students and scholars within VU and externally, including MIT, UPenn and Georgia Tech. He is very enthusiastic in both research and teaching for undergraduates. He has supervised more than 50 undergraduate students in the past and many of them have been awarded VU awards for research and national recognition, including Villanova VURF fellows, Falvey Scholars, NASA internship, NSF REU research fellows, and DOE internships.